Journal of the European Ceramic Society xxx (xxxx) xxx

Contents lists available at ScienceDirect

Journal of the European Ceramic Society

journal homepage: www.elsevier.com/locate/jeurceramsoc

Layered $Y_3Al_5O_{12}$:Pr/$Gd_3(Ga,Al)_5O_{12}$:Ce optical ceramics: Synthesis and photo-physical properties

Francesca Cova [a], Jan Hostaša [b], Andreana Piancastelli [b], Laura Esposito [b], Alberto Paleari [a], Anna Vedda [a], Roberto Lorenzi [a,*]

[a] Department of Materials Science, University of Milano – Bicocca, Via Cozzi 55, 20125 Milan, Italy
[b] CNR ISSMC, Institute of Science, Technology and Sustainability for Ceramics, Via Granarolo 64, 48018 Faenza, Italy

ARTICLE INFO

Keywords:
Transparent ceramics
Layered structure
Scintillators
GGAG:Ce
YAG:Pr
Hot isostatic pressing
Luminescence
Diffusion length

ABSTRACT

We report a study of composite scintillating ceramics based on coupled layers of two different garnets, namely Ce-doped gadolinium gallium aluminium (GGAG:Ce) and Pr-doped yttrium aluminium (YAG:Pr), fabricated by hot isostatic pressing. Two samples were prepared, with different GGAG:Ce layer thickness, 120 μm and 690 μm respectively, but with a comparable overall thickness of 1.4 mm. The key finding is that the material architecture strongly determines the scintillation response. The radioluminescence is that expected from the irradiated material when a thick layer of ceramic is exposed to X-rays. Conversely, exposing a thin layer allows a non-null probability —about 0.3% for 120 μm of GGAG— of finding an X-ray photon in the underlying layer, and thus radioluminescence from both materials is recorded. We believe these results can extend the potential of layered optical ceramics for advanced devices, such as energy- and direction-sensitive X-ray detectors.

1. Introduction

Scintillating materials are widely used for ionizing radiation detection applications, such as dosimetry [1] and nuclear medicine [2,3], particle identification [4], and X-ray-based security [5,6]. Remarkable advances in the scintillation science have brought the material performance close to the intrinsic limits, while the requirements have become increasingly demanding [7], mainly in terms of fast luminescence response, good luminosity, high density, and optimal radiation hardness. Current research aims at the development of highly specialized scintillators and innovative detector designs, by combining different scintillator architectures to achieve the best performance [8]. Single crystals are the dominant bulk form of inorganic scintillators; however, the limitations imposed by manufacturing processes have led to the search and development of alternative and more easily processable media such as glasses and plastics [9–13]. A new approach to overcome the limitations of single monolithic bulk materials as the sole means of energy-to-light conversion medium is to use functionalised heterostructures in which more than a single material works in synergy. Due to its potential to achieve unparalleled properties and its inherent flexibility to tailor the detector performance to the application requirements, this concept has recently gained popularity. Therefore, the controlled spatial non-uniformity, material, and shape of heterostructured radiation detectors has led to novel concepts such as the partitioning of the energy deposited in the material during the scintillation mechanism [14,15].

Transparent ceramics are an emerging class of materials with interesting optical and scintillating properties combined with a relative ease of fabrication. They are used in laser and scintillation applications requiring large volumes, while composite materials are used in an attempt to couple specific functionalities of the different phases [16]. In particular, advances in the sintering technique of crystalline nano- or micro-grains into bulk ceramics of high optical quality have led optical ceramics to become highly competitive with single crystals [17–19], due to their lower cost of production [20,21], lower sintering temperature, and the ability to uniformly incorporate a much higher concentration of activator species [22]. In addition, the ease and flexibility of shaping makes ceramic technology extremely attractive, especially when a specific geometry cannot be achieved by single crystal growth [23,24], such as multilayer structures for scintillation and laser operation [25–27]. In the recent years, the investigation of ceramic materials brought a significant development in the preparation processes associated with performance optimisation [28]. Some of the findings from single crystal research are being applied to optical ceramics, such as co-doping to

* Corresponding author.
E-mail address: roberto.lorenzi@unimib.it (R. Lorenzi).

https://doi.org/10.1016/j.jeurceramsoc.2023.07.037
Received 13 April 2023; Accepted 17 July 2023
Available online 20 July 2023

remove slow components in the scintillation time decay [29,30].

In this context, garnets are being studied as very promising materials in the field of scintillation, due to their optical transparency and the possibility to easily incorporate luminescent rare-earth (RE) ions into their lattice. Recently, $Gd_3(Ga, Al)_5O_{12}$ (GGAG) multicomponent garnet has attracted much interest due to its excellent scintillation and luminescence properties. GGAG garnet crystals are now produced with a light output of around 50000 ph/MeV, bridging the gap between oxides and the traditionally very efficient halide scintillators. When doped with Ce, it also has a relatively short scintillation lifetime (a few tens of nanoseconds), giving it superior timing performance compared to other garnets [31–34]. GGAG has a cubic crystalline structure, and it is therefore suitable for sintering in the form of transparent polycrystalline ceramics [35], opening up wide prospects for new geometries and shapes, as well as for compositional control of the material [36–38].

In the present work, we design a novel layered $Y_3Al_5O_{12}$:Pr/$Gd_3Ga_3Al_2O_{12}$:Ce (YAG:Pr/GGAG:Ce) composite scintillating ceramic, consisting of a two-phase mixture with different luminescent activators, prepared by a combined approach of conventional pressureless sintering in air followed by hot isostatic pressing (HIP), which did not require additional cutting or bonding processes as schematically shown in Fig. 1a. These materials couple the scintillation performances of YAG garnets for X-ray detection [17,39–42] with the high thermal neutron cross-section of Gd inside the GGAG matrix making them suitable for neutron detection [4,43,44]. Chen et al. [45] already reported on the synthesis and characterization of a composite ceramic YAG:Cr/GGAG:Ce with layered structure for full luminescence spectrum applications. In addition, layered ceramics have been widely used in solid-state lasers [46] and light emitting diodes [47,48], and proposed for positron emission tomography with depth-of-interaction (PET-DOI) scanners [2,49–51] and particle discrimination in mixed radiation fields [52–54]. Here, we choose the doping with Pr^{3+} and Ce^{3+} ions to provide a bright luminescence and a fast scintillation response. We fabricated two samples with straight separation of the two layers and different relative thickness with the aim of disclosing the crucial role of the material design on the resulting scintillation signal. Structural and compositional studies were carried out by scanning electron microscopy, energy dispersive X-ray analysis, and X-ray diffraction, whereas their optical and scintillation properties were evaluated by UV–visible absorption measurements, and by micro-photoluminescence (μ-PL) and radio-luminescence (RL) spectroscopies. Furthermore, as sketched in Fig. 1b, we took advantage of the adjustable geometry of the layered structure to control the penetration depth of the incident ionizing radiation and to selectively trigger the scintillation emission from one or both layers.

2. Material and methods

2.1. Sample preparation

Ceramic samples with the composition GGAG:0.3% Ce and YAG:0.2% Pr were produced by reaction sintering from commercial oxide powders. High purity oxide powders were mixed in the stoichiometric ratio corresponding to $Ce_{0.009}Gd_{2.991}Al_2Ga_3O_{12}$ and $Pr_{0.006}Y_{2.994}Al_5O_{12}$, respectively, and 0.5 wt% of TEOS (tetraethyl orthosilicate) was used as a sintering aid in both mixtures. The powders were mixed by ball milling in ethanol with alumina balls, the ethanol was extracted by a rotary evaporator and the powder was placed into a dryer for 24 h at 80 °C. Afterwards, the two powders mixtures were sieved and each was uniaxially pressed into discs of different thickness in order to produce the desired structures. The YAG:Pr and GGAG:Ce parts were then stacked and pressed together into one piece by cold isostatic pressing (CIP) at 250 MPa. This approach was earlier applied for layered YAG/YAG:Yb composite transparent ceramics [26]. The samples were heat treated in air at 1600 °C with soaking time of 4 h. This led to the elimination of organic residues, formation of the desired

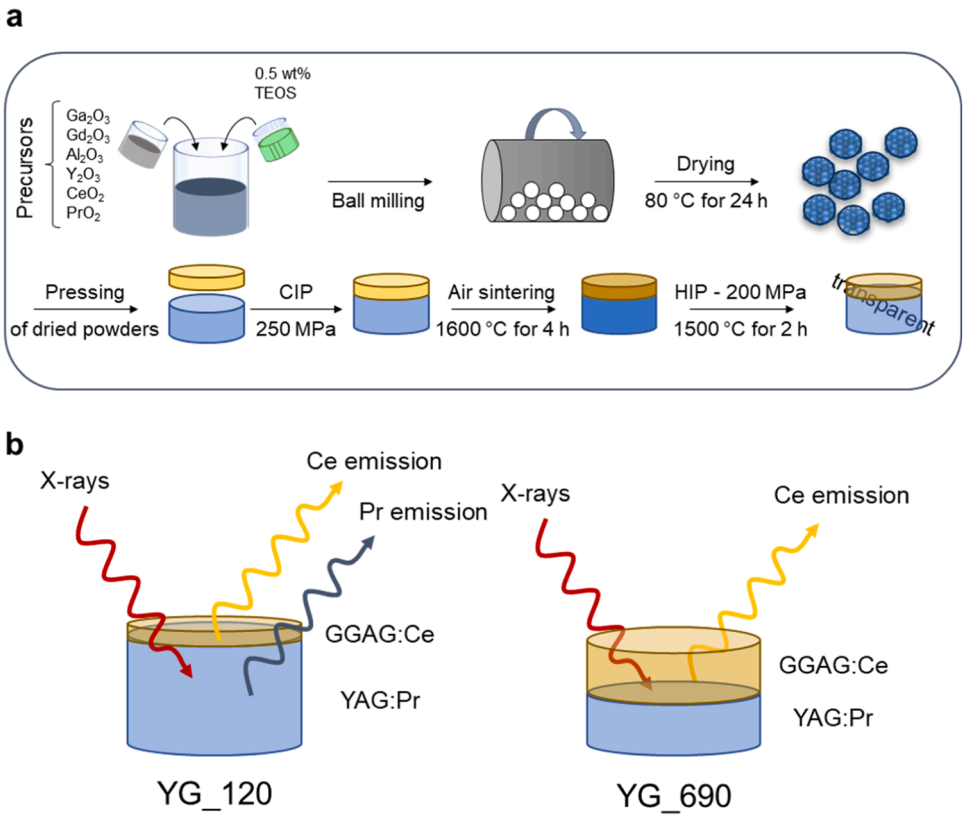

Fig. 1. (a) Synthesis procedure for composite ceramics. (b) Sketch of the interaction of X-rays with the composite ceramics by varying the geometry of the layered structure.

phases and to a microstructure with a closed porosity. Hot isostatic pressing in argon was then performed to promote full densification of the material: the applied pressure was 200 MPa, soaking temperature 1500 °C and soaking time 2 h. The sintering conditions followed those for GGAG:Ce, studied more in detail in [55]. Sintered samples were polished with diamond pastes and sprays of grade from 30 μm down to 0.25 μm. After polishing, the two tested samples had the respective thickness of the GGAG:Ce layer of about 120 μm (sample YG_120) and 690 μm (sample YG_690).

2.2. Structural characterization

Phase composition of the sintered samples was analysed by X-ray diffraction (XRD) of the polished surfaces. Room temperature measurements were performed with D8 Advance diffractometer (Bruker). The microstructure of the ceramics was analysed with a field emission scanning electron microscope (FE-SEM) model SIGMA (Zeiss) equipped with an Energy Dispersive X-ray (EDX) analyser (INCA Energy 300, Oxford Instruments Analytical).

2.3. Optical and scintillation measurements

Optical absorption spectroscopy was carried out using a Lambda 950 UV/VIS (Perkin Elmer) double beam spectrometer equipped with a Spectralon coated integrating sphere to collect also the scattered light. Refractive indices have been measured by a prism coupling refractometer Metricon 2010 working at 633 nm with an uncertainty lower than 10^{-3}.

Confocal micro-fluorescence profiles were recorded at room temperature by a spectrometer (Labram, Jobin-Yvon), using an external Ar-ion laser at 488 nm as excitation source, focusing the beam on a circular spot through the optics of a microscope (Olympus) and an objective with magnification 10x. The micro-fluorescence spectra were collected in back-scattering configuration through a Peltier-cooled silicon CCD (charge coupled device) detector, after a monochromator equipped with a 300 grooves/mm grating.

Radio-luminescence measurements were performed by exciting the samples by unfiltered X-ray irradiation using a Philips PW2274 X-ray tube, equipped with a tungsten target and a beryllium window and operated at 20 kV. At this operating voltage, X-rays are produced by the *Bremsstrahlung* mechanism superimposed to the L and M transition lines of tungsten due to the impact of electrons generated through a thermionic effect and accelerated onto the tungsten target. The radioluminescence was collected using a custom apparatus featuring a liquid nitrogen-cooled, back-illuminated, and UV-enhanced CCD detector (Jobin-Yvon Symphony II) coupled to a monochromator (Jobin-Yvon Triax 180) with a 100 lines/mm grating.

3. Results and discussion

SEM micrographs of polished sections of the two YAG:Pr/GGAG:Ce layered ceramics, showing a clean and defect-free interface, are shown in Figs. 2a and 2b, for YG_120 and YG_690, respectively. The images were obtained by collecting backscattered electrons, so the darker regions correspond to materials with lower density. Thus the lighter and darker parts belong to GGAG:Ce and YAG:Pr, which have densities of 6.7 and 4.3 g/cm^3 respectively [41,56]. As expected from the synthesis parameters, the GGAG layer thickness for samples YG_120 and YG_690 is 120 ± 20 μm and 690 ± 10 μm, respectively, according to the SEM image analysis, although both samples have a similar total thickness of 1380 ± 20 μm. The thickness of the layer with interdiffused ions is similar for both samples, although the YAG/GGAG relative thickness is significantly different. This characteristic can be further analysed by the atomic distribution over the interlayer. The EDX mapping analysis following the Y, Al, and Ga profiles is shown in Figs. 2c and 2d. The data were taken along a 200 μm line across the cross section of the ceramic, centred on the interface between the two materials. The initial and final values of the profiles match with the expected atomic composition of $Y_3Al_5O_{12}$ (Y=15 and Al=25 at%) and $Gd_3Ga_3Al_2O_{12}$ (Gd=15, Ga=15, and Al=10 at%). The profile has the typical sigmoidal behaviour related to atomic interdiffusion from coupled materials. These profiles can be fitted with a variety of functions, which usually correspond to cumulative distribution functions [57]. In our case, the concentration c as a function of the position x is satisfactorily fitted by a logistic distribution:

$$c(x) = c_{in} + \frac{c_{fin}}{1 + e^{-\frac{(x-x_0)}{\pm s}}} \quad (1)$$

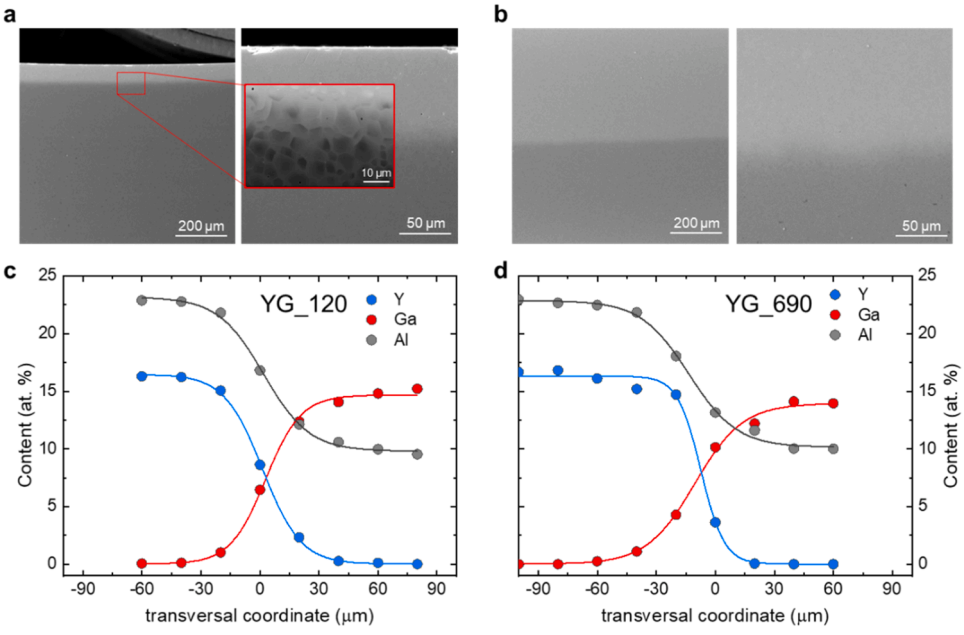

Fig. 2. (a, b) SEM micrographs of the transversal section of YG_120 and YG_690 respectively and enlargements of the interdiffused region. Inset of panel (a): SEM image of grain boundary diffusion for YG_120. (c, d) EDX profiles of the content of Y, Ga, and Al for YG_120 and YG_690 respectively (full symbols). Solid lines represent the fit of the experimental data with the logistic distribution reported in Eq. (1).

where c_{in} and c_{fin} are the initial and final concentrations, x_0 corresponds to the midpoint of the curve, and s is the steepness parameter. The sign before the s parameter is positive for increasing profiles and negative for decreasing profiles. All profiles were fitted simultaneously by a global fit. The global fit kept s as a common parameter and c_{in}, c_{fin}, and x_0 as free parameters for each profile. The steepness parameter provides a measurement of the diffusion length and it is equal to 9.7 ± 0.5 μm irrespective of the GGAG layer thickness and the diffusing ion considered. This length qualitatively agrees with the RE diffusion distance in similarly treated YAG optical ceramics [58]. The Boltzmann-Matano method can be used for a more accurate determination of the diffusion parameters [59]. Eq. 1 is invertible and, due to its symmetry, the Matano interface lies at x_0. Thus, the inverse function $x(c)$ was used to numerically solve the Boltzmann-Matano equation which gives the value of the concentration-dependent diffusion coefficient $D(c)$:

$$D(c^*) = \frac{-\frac{1}{2t}\int_{c_{in}}^{c^*}(x(c) - x_0)dc}{\left.\frac{dc}{dx}\right|_{c=c^*}} \quad (2)$$

where c^* may run from c_{in} to c_{fin}, and t is the total amount of annealing time. The diffusion coefficient at the Matano interface is equal to (6.0 ± 0.5)·10^{-15} m^2/s which is about three order of magnitude less than the diffusion coefficient of Ga in bulk YAG [60]. Indeed, this is consistent with diffusion processes dominated by grain boundary diffusion, as in the case of optical ceramics, where D for annealing at ≈ 1500 °C is of the order of 10^{-15} - 10^{-16} m^2/s [58,61]. In ceramics, the grain boundary diffusion may also be enhanced by the presence of sintering aids, as reported for Nd in YAG [62]. Compared to YAG-YAG:Yb layered ceramics [26,27], in our samples the grain size is smaller and the interdiffusion layer thickness is lower, as illustrated in the inset of Fig. 2a for the YG_120 sample; however, this can be most easily ascribed to the differences of the sintering processes (sintering in air and HIP compared to single-step vacuum sintering at a higher temperature and longer soaking times, 16 h and more at 1735 °C, that promote diffusion).

The crystal structure of the samples was analysed by XRD, which provides a first insight into the response to X-ray interaction of the two samples, characterized by the different geometry of their layers. The X-ray diffraction patterns of both sides of the YAG:Pr/GGAG:Ce composite ceramics are shown in Fig. 3a and b, together with the expected reflection for pure garnet phases. All the observed peaks can be indexed to the standard diffraction patterns of pure $Gd_3Al_3Ga_2O_{12}$ (JCPDS n. 46–0448) and pure $Y_3Al_5O_{12}$ (JCPDS n. 33–0040) respectively, indicating that pure crystalline structures of YAG and GGAG have formed in the two layers and no other phases were detected. Importantly, the recorded diffractograms are affected by the stacking order and relative thickness of the layers. If the side that is exposed to X-rays is a thick layer, then the pattern that is collected can be attributed to that phase. This is the case for sample YG_690, where only YAG or GGAG phases can be detected in accordance with the layer facing the X-ray source. Conversely, for YG_120, if the thick YAG layer is measured, only the reflection of YAG can be detected, whereas if the sample is measured upside down - exposing the thin GGAG layer to X-rays - then the diffraction shows signals from both GGAG and YAG phases.

The optical absorption spectra are shown in Fig. 4a and b. As expected, the spectra show all the absorption characteristics of GGAG:Ce and YAG:Pr weighted by the respective thickness. The main features can be indexed as follows. Two broad absorption bands, evidenced by red arrows, related to the Ce^{3+} 4f – $5d_1$ and 4f – $5d_2$ transitions are clearly visible at around 440 nm and 340 nm, respectively. The presence of Gd^{3+} 4f – 4f absorption lines from the $^8S_{7/2}$ ground state to the ^6P, ^6I, and ^6G excited state group levels at around 310 nm, 275 nm, and 210 nm respectively, are more clearly visible in the YG_690 absorption spectrum. Finally, absorption bands related to Pr^{3+} transitions are indicated by blue arrows and can be attributed to 4f – 5d transitions at around 235 nm and 285 nm and to 4f – 4f absorption lines in the red spectral region, assigned to transitions from the $^3H_4$ ground state level to the $^3P_0$, $^3P_1$ and $^3P_2$ levels (enlarged in the insets). As mentioned above, the intensities of absorption bands are directly related to the thickness of the corresponding absorbing layer. As a result, absorption features associated with GGAG:Ce are better appreciated in sample YG_690, whereas YAG:Pr transitions are well distinguished in YG_120. This effect is evident for the Gd^{3+} 4f – 4f Laporte forbidden transitions which are almost absent in YG_120 but clearly visible in YG_690.

In addition, the absorption spectra are characterised by a significant baseline, which in the red spectral region is approximately 0.25 absorbances, corresponding to a transmission of 56%. These values are much higher than the expected reflection losses. The reflectance R can be quantified using the Fresnel equation at normal incidence, for which we have at each interface:

$$R = \left|\frac{n_1 - n_2}{n_1 + n_2}\right|^2 \quad (3)$$

where n_1 and n_2 are the refractive indices of the two media. Applying Eq. 3 to all the interfaces in our system (i.e. air/GGAG/YAG/air) and assuming n_{Air}= 1 and using the measured values at 633 nm of n_{YAG}= 1.83 and n_{GGAG}= 1.92, we obtain a reflection loss of 17%, corresponding to 0.082 absorbances. The remaining losses must therefore be caused by scattering phenomena originated by the presence of residual pores or secondary phases in the optical ceramic. This is also supported by the significant growth of the baseline with decreasing

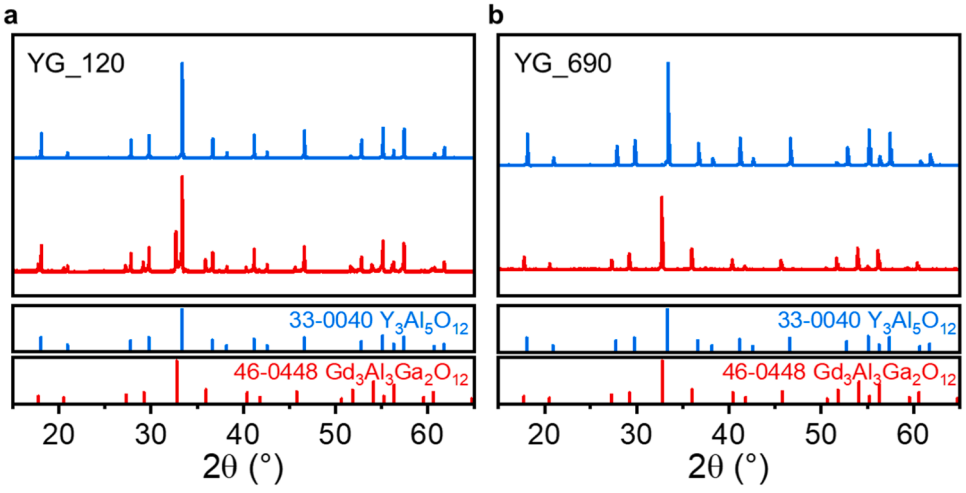

Fig. 3. XRD patterns of the two sides of YG_120 (a) and YG_690 (b): blue lines for YAG:Pr side and red lines for GGAG:Ce face.

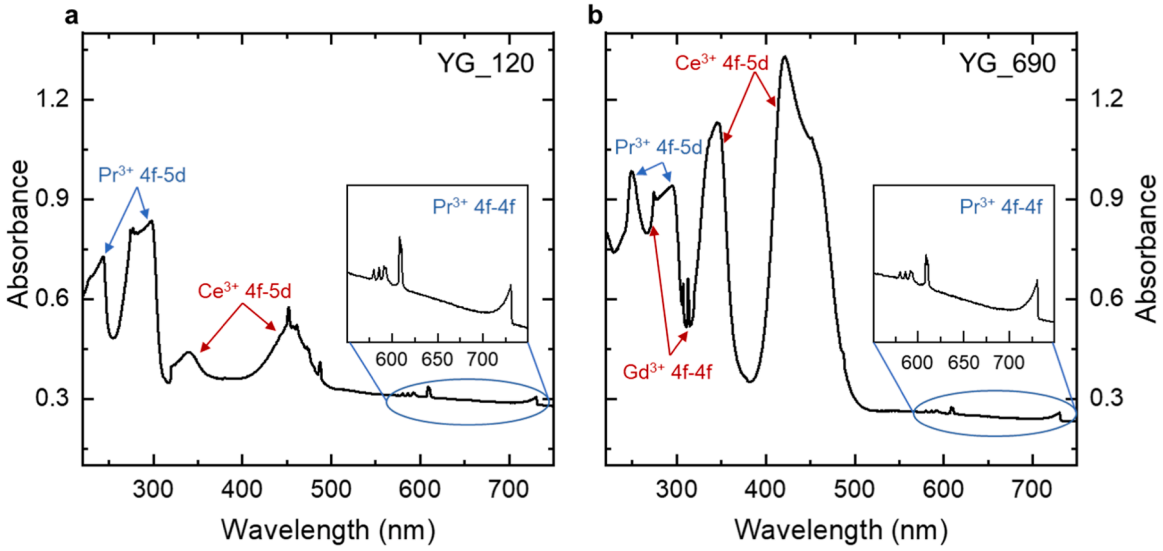

Fig. 4. Optical absorption spectra of YG_120 (a) and YG_690 (b): in the insets, the enlargements of 4f – 4f absorption lines of Pr^{3+} ions in the 600 – 800 nm region are shown.

wavelength, as predicted by Rayleigh scattering. The SEM analysis showed the presence of a few pores and a small number of Al_2O_3 grains in the YAG:Pr part. In the case of optical absorption, the characteristic absorption features of the individual ceramic layers cannot be separated from each other, regardless of the thickness of the layers.

Crucially, μ-PL and RL measurements show that, as long as the

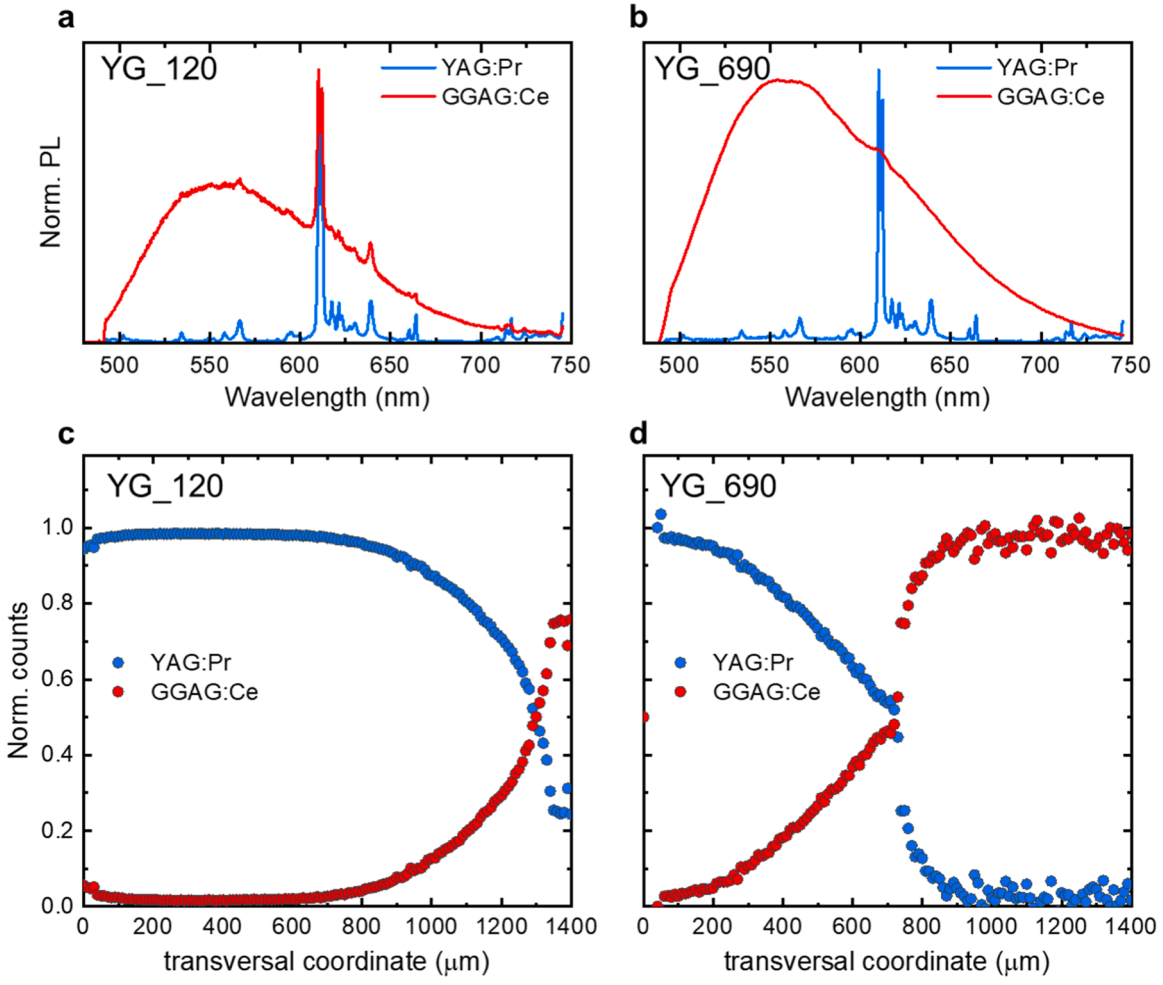

Fig. 5. (a, b) μ-PL spectra excited at 488 nm of YAG:Pr and GGAG:Ce for YG_120 and YG_690 respectively, collected at the two extremities of a scan across the transversal section of the samples. (c, d) μ-PL profiles of the layered ceramics interface.

excitation depth of the incident radiation is lower than the thickness of the irradiated layer, it is possible to selectively detect the light emitted by one of the two layers. Indeed, the μ-PL spectra of YAG:Pr and GGAG:Ce recorded at the two ends of a line scan across the interface are reported in Fig. 5a and b, showing the typical emission features of Pr^{3+} and Ce^{3+} ions, respectively. In fact, the excitation laser line at 488 nm is able to efficiently excite both Pr^{3+} through the f-f transitions ($^3H_4 \rightarrow {}^3P_0$) and Ce^{3+} through the transition from the $4f_1$ ground level to the lowest $5d_1$ excited level [63]. The emission of Pr^{3+} ions is characterised by several narrow lines in the 500 – 600 nm spectral region, ascribed to the parity forbidden 4f – 4f transitions, whereas Ce^{3+} ions have the characteristic broad emission band at around 535 nm of the allowed 5d – 4 f transition.

Similarly to XRD patterns, the stacking conformation plays an important role in detecting the two signals. In fact, the spectra related to pure YAG:Pr can be recorded on both YG_120 and YG_690 because its thickness is sufficiently high to avoid interactions between the excitation laser and the complementary GGAG:Ce layer. Conversely, in sample YG_690, but not in YG_120, the pure GGAG:Ce spectrum is observed. Transversal scan of coupled materials with different refractive indices is affected by waveguiding effects where out-of-focus contributions on the order of tens of microns can be detected [64,65]. Thus, for the YG_120 sample, it is possible to detect residual signal from the YAG:Pr layer even when probing the GGAG:Ce layer. However, the cross-sectional μ-PL profile of the coupled material still presents a clear separation of the two layers. Fig. 5c and d report the intensities of the two emissions, as a function of the excitation position across the interface, normalized as follows. The intensity of Ce emission has been evaluated at 550 nm, whereas that of Pr at 610 nm removing the baseline due to the superposition of the two signals: then the intensity of each emission has been normalized for the total intensity calculated at each position of the excitation along the scan. In contrast to EDX experiments, μ-PL profiles are strongly affected by spurious effects from unwanted out-of-focus signals, which prevent a deep analysis of the interdiffusion layer. However, the profiles give a GGAG:Ce layer of 680 ± 60 μm and 120 ± 50 μm for YG_690 and YG_120 sample, respectively, in agreement with SEM images.

Fig. 6a and b report the RL emission spectra of the two sides of the YAG:Pr/GGAG:Ce layered ceramics. The emitted light is collected from the same side facing the X-ray irradiation. Similarly to XRD experiments, it depends on the thickness of the first layer interacting with the X-rays whether spectral features relating to only one or both layers are observed. Therefore, by exciting the YAG:Pr layer the resulting RL spectra are characterised by the main broad emission bands at around 310 nm and 375 nm, and the emission lines in the 500 – 600 nm spectral region attributed to the allowed 5d - 4f and to the forbidden 4f – 4f transitions of Pr^{3+} ions, respectively. The YAG:Pr layer is thick enough to prevent X-ray penetration into the GGAG:Ce layer in both the YG_120 and YG_690 samples. Therefore, the spectra collected by exciting the YAG:Pr layer are very similar for both samples. Conversely, the X-ray irradiation of the GGAG:Ce side results in different RL spectra for the two samples. The pure GGAG:Ce spectrum can only be detected in sample YG_690 where the only emission is the characteristic band of the 5d – 4 f transition of Ce^{3+} ions at around 535 nm. Instead, emissions from both the Pr and Ce-related bands are seen in sample YG_120. This result shows that a top layer of ≈ 120 μm of GGAG is thin enough to allow X-ray penetration down to the second layer. The X-ray penetration depth in these systems can be evaluated by simple calculations. We determined the linear attenuation coefficient $\mu(E)$ as a function of photon energy from tabulated data (from the NIST database [66]), which is the inverse of the X-ray attenuation depth: $\lambda(E) = 1/\mu(E)$. The penetration depth describes the exponential decay of the radiation intensity, I, as the beam passes through the medium along the x direction:

$$I(E,x) = I_0(E)e^{-x\cdot\mu(E)} = I_0(E)e^{-x/\lambda(E)} \quad (4)$$

The depth of penetration depends on the energy of the X-rays. In general, more energetic beams correspond to greater penetration, as reported in Fig. 6c (green line). We must then consider that the X-ray

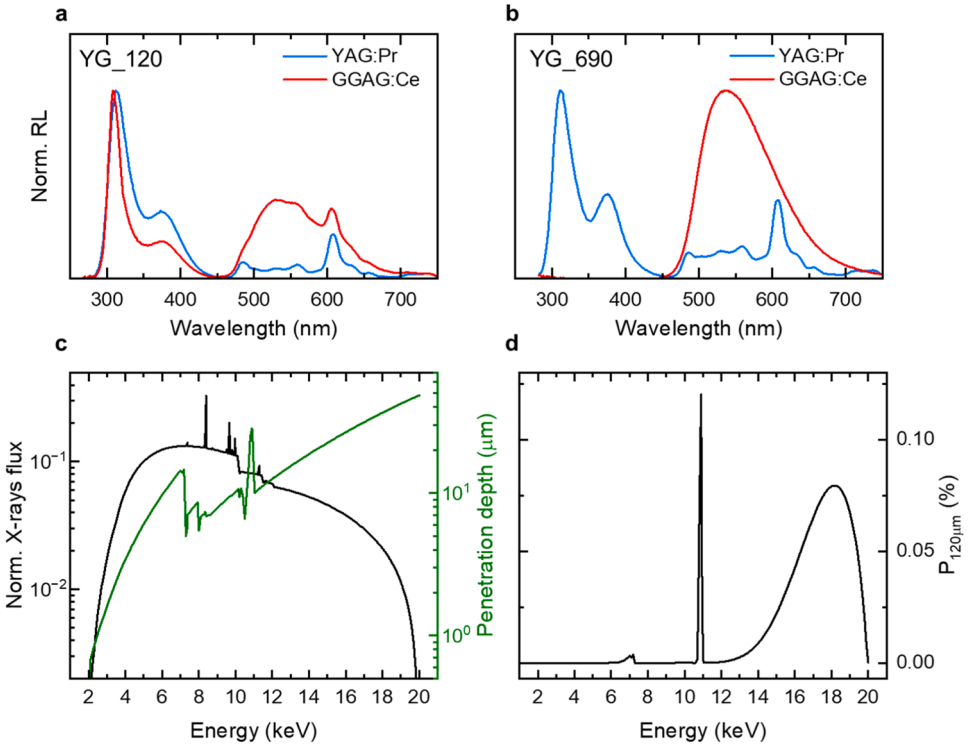

Fig. 6. (a, b) RL spectra of the two sides of the layered ceramics YG_120 and YG_690, respectively, excited by soft X-rays. (c) Normalized spectral distribution of X-rays generated by Bremsstrahlung by an X-ray tube operating at 20 kV with tungsten target (black line). X-ray penetration depth evaluated from NIST database (green line). (d) Probability of finding an X-ray photon of a given energy beyond a GGAG layer of thickness 120 μm.

source is not monochromatic, but results from the superposition of the continuous *Bremsstrahlung* spectrum and the characteristic sharp lines of the tungsten target. Fig. 6c (black line) shows the area-normalised spectral distribution (in ph/s) of a tube operating at 20 kV and with a tungsten target as the one used in our RL experiments. If we consider this spectral output as the initial radiation intensity I_0 in Eq. (4), then we can calculate the intensity attenuation after the X-ray has passed through a layer of thickness x as a function of the photon energy E. This attenuation corresponds to the probability P of finding an X-ray of a given energy E beyond a layer of thickness x. This probability is shown in Fig. 6d for a GGAG layer of 120 μm, which simulates the condition of the sample YG_120. Interestingly, the photons at the maximum of the *Bremsstrahlung* distribution (at about 7.1 keV) are completely stopped with a $P \leq 0.0025\%$, but in correspondence of the tungsten sharp L-line (at about 8.4 keV) there is a spike where $P \approx 0.12\%$. Furthermore, the combination of longer penetration depths with a significant spectral output of the tube at higher photon energies leads to a non-null probability of finding photons at $E > 12$ keV below 120 μm of GGAG. As in the case of the tungsten L-line, the probability in this energy range is of the order of 0.01–0.1%. Although these numbers appear small, it should be remembered that the probability of finding photons of any energy is given by the integral over all the available energies. Indeed, the integral of the curve in Fig. 6d is 0.32. Remarkably, the intensity drops in this range are still able to excite the underlying layer, and the resulting RL signal is well above the detection limit of our apparatus. Even in XRD analysis, which has more stringent requirements for the detection of signals from low X-ray intensities, a reasonable detection limit for standard instruments is at 0.1% of I_0 [67]. Performing the same calculations for sample YG_690, the probability of finding an X-ray photon beyond a 690 μm thick layer of GGAG is $2{\cdot}10^{-9}$, evidencing the exponential nature of the attenuation process. This probability can be considered to be zero; in agreement with RL experiments where the pure GGAG:Ce and YAG:Pr spectra are detected depending on the side exposed to the X-ray source. Crucially, the different RL response of YG_120 and YG_690 leaves room for possible energy transfer between the two layers: specifically, the higher RL intensity in the 500 – 600 nm spectral region of YAG:Pr in sample YG_690 could result from the resonance between the 5d-4 f emission of Pr^{3+} and the 4 f-$5d_2$ absorption of Ce^{3+}. However, a recognizable RL detection of Ce^{3+} is only possible when the YAG:Pr layer above the GGAG:Ce is thin enough to allow direct excitation by residual X-rays passing through the first layer without the need of energy transfer. This confirms that our synthetic approach to the fabrication of layered ceramics leads to an efficient separation of the scintillation properties of the two garnets as far as the thicknesses involved are high enough. The resulting material is a composite scintillator with controlled absorption/emission properties and the architecture of its layers plays a crucial role in determining the complementarity of the RL properties of the two constituent phases.

4. Conclusions

In summary, we realized a composite garnet ceramic scintillator made of YAG:Pr and GGAG:Ce with two different architectures and demonstrated that the material geometry is a key factor in controlling the scintillation response. Specifically, we experimentally proved that the relative thickness of the two layers comprising the composite ceramics determines its capability of fully absorb the incident high-energy ionizing radiation, and therefore its scintillation emission. In addition, the two different RE luminescent centers are accommodated individually in different layers to achieve complementary spectral components and avoid mutual interaction of co-doped luminescent ions in the same confined crystalline structure. Indeed, RE ions emitting in well-distinguished spectral regions allow to selectively identify the scintillating layer interacting with the ionizing radiation. As a result, the tunable architecture of our layered optical ceramics opens perspective for the improvement of the spatial resolution in PET-DOI scanners and can be successfully implemented for phoswich applications and particle discrimination in mixed radiation fields.

Declaration of Competing Interest

The authors declare that they have no known competing financial interests or personal relationships that could have appeared to influence the work reported in this paper.

References

[1] I. Veronese, N. Chiodini, S. Cialdi, E. d'Ippolito, M. Fasoli, S. Gallo, S. La Torre, E. Mones, A. Vedda, G. Loi, Phys. Med. Biol. 62 (2017) 4218.
[2] M. Ito, S.J. Hong, J.S. Lee, Biomed. Eng. Lett. 1 (2011) 70–81.
[3] P. Lecoq, Nucl. Instrum. Methods Phys. Res. Sect. A Accel. Spectrom. Detect. Assoc. Equip. 809 (2016) 130–139.
[4] G. Zorloni, L. Cremonesi, F. Cova, A. Vedda, M. Caresana, Radiat. Meas. 135 (2020), 106370.
[5] J. Glodo, Y. Wang, R. Shawgo, C. Brecher, R.H. Hawrami, J. Tower, K.S. Shah, Phys. Procedia 90 (2017) 285–290.
[6] A. Arodzero, S. Boucher, J. Hartzell, S.V. Kutsaev, R.C. Lanza, V. Palermo, S. Vinogradov, V. Ziskin, High speed, low dose, intelligent X-ray cargo inspection, 2015 IEEE Nuclear Science Symposium and Medical Imaging Conference (NSS/MIC), IEEE2015, pp. 1–7.
[7] C. Dujardin, E. Auffray, E. Bourret-Courchesne, P. Dorenbos, P. Lecoq, M. Nikl, A. Vasil'Ev, A. Yoshikawa, R.-Y. Zhu, IEEE Trans. Nucl. Sci. 65 (2018) 1977–1997.
[8] J. LLorca, V.M. Orera, Prog. Mater. Sci. 51 (2006) 711–809.
[9] R. Lorenzi, N.V. Golubev, M.Z. Ziaytdinova, V. Jarý, V. Babin, G.E. Malashkevich, A. Paleari, V.N. Sigaev, M. Fasoli, M. Nikl, Opt. Mater. 78 (2018) 247–252.
[10] F. Cova, M.T. Lucchini, K. Pauwels, E. Auffray, N. Chiodini, M. Fasoli, A. Vedda, Phys. Rev. Appl. 11 (2019), 024036.
[11] A. Vedda, N. Chiodini, D. Di Martino, M. Fasoli, F. Morazzoni, F. Moretti, R. Scotti, G. Spinolo, A. Baraldi, R. Capelletti, Chem. Mater. 18 (2006) 6178–6185.
[12] J. Perego, I. Villa, A. Pedrini, E. Padovani, R. Crapanzano, A. Vedda, C. Dujardin, C. X. Bezuidenhout, S. Bracco, P. Sozzani, Nat. Photonics 15 (2021) 393–400.
[13] F. Carulli, F. Cova, L. Gironi, F. Meinardi, A. Vedda, S. Brovelli, Adv. Opt. Mater. (2022) 2200419.
[14] P. Krause, E. Rogers, M.D. Birowosuto, Q. Pei, E. Auffray, A.N. Vasil'ev, G. Bizarri, Heliyon 8 (2022), e09754.
[15] F. Pagano, N. Kratochwil, M. Salomoni, M. Pizzichemi, M. Paganoni, E. Auffray, Phys. Med. Biol. 67 (2022), 135010.
[16] A. Yoshikawa, K. Kamada, S. Kurosawa, Y. Yokota, A. Yamaji, V.I. Chani, Y. Ohashi, M. Yoshino, J. Cryst. Growth 498 (2018) 170–178.
[17] A. Ikesue, Y.L. Aung, Nat. Photonics 2 (2008) 721–727.
[18] N. Cherepy, J. Kuntz, Z. Seeley, S. Fisher, O. Drury, B. Sturm, T. Hurst, R. Sanner, J. Roberts, S. Payne, Transparent ceramic scintillators for gamma spectroscopy and radiography. Hard X-Ray, Gamma-Ray, and Neutron Detector Physics XII, SPIE,, 2010, pp. 69–73.
[19] S. Liu, J.A. Mares, X. Feng, A. Vedda, M. Fasoli, Y. Shi, H. Kou, A. Beitlerova, L. Wu, C. D'Ambrosio, Adv. Opt. Mater. 4 (2016) 731–739.
[20] D.J. Wisniewski, L.A. Boatner, J.S. Neal, G.E. Jellison, J.O. Ramey, A. North, M. Wisniewska, A.E. Payzant, J.Y. Howe, A. Lempicki, IEEE Trans. Nucl. Sci. 55 (2008) 1501–1508.
[21] C. Greskovich, S. Duclos, Annu. Rev. Mater. Sci. 27 (1997) 69–88.
[22] J. Xu, L. Fan, Y. Shi, J. Li, J. Xie, F. Lei, Opt. Mater. 36 (2014) 1954–1958.
[23] L. Ge, J. Li, Z. Zhou, H. Qu, M. Dong, Y. Zhu, T. Xie, W. Li, M. Chen, H. Kou, Opt. Mater. Express 4 (2014) 1042–1049.
[24] V. Gorbenko, E. Zych, T. Voznyak, S. Nizankovskiy, T. Zorenko, Y. Zorenko, Opt. Mater. 66 (2017) 271–276.
[25] Z. Hu, X. Chen, D. Ding, M. Cao, Y. Shi, H. Kou, H. Chen, T. Xie, L. Wu, Y. Pan, J. Am. Ceram. Soc. 100 (2017) 5593–5600.
[26] J. Hostaša, V. Biasini, A. Piancastelli, M. Vannini, G. Toci, Opt. Eng. 55 (2016), 087104-087104.
[27] J. Hostaša, G. Toci, L. Esposito, B. Patrizi, M. Vannini, A. Pirri, F. Picelli, A. Piancastelli, M. Pucci, V. Biasini, Planar and rectangular ceramic Yb: YAG laser waveguides. Fiber Lasers and Glass Photonics: Materials through Applications III, SPIE,, 2022, pp. 6–12.
[28] M. Suárez, A. Fernández, R. Torrecillas, J.L. Menéndez, Sintering to transparency of polycrystalline ceramic materials, Sintering of Ceramics-New Emerging Techniques, Citeseer 2012.
[29] M. Tyagi, H.E. Rothfuss, S.B. Donnald, M. Koschan, C.L. Melcher, IEEE Trans. Nucl. Sci. 61 (2014) 297–300.
[30] V. Babin, P. Bohacek, L. Grigorjeva, M. Kučera, M. Nikl, S. Zazubovich, A. Zolotarjovs, Opt. Mater. 66 (2017) 48–58.
[31] A. Yoshikawa, Y. Fujimoto, A. Yamaji, S. Kurosawa, J. Pejchal, M. Sugiyama, S. Wakahara, Y. Futami, Y. Yokota, K. Kamada, Opt. Mater. 35 (2013) 1882–1886.
[32] A. Yoshikawa, K. Kamada, S. Kurosawa, Y. Shoji, Y. Yokota, V. Chani, M. Nikl, J. Lumin. 169 (2016) 387–393.
[33] K. Kamada, T. Yanagida, T. Endo, K. Tsutumi, Y. Usuki, M. Nikl, Y. Fujimoto, A. Yoshikawa, 2-inch size single crystal growth and scintillation properties of new scintillator; Ce: Gd 3 Al 2 Ga 3 O 12, 2011 IEEE Nuclear Science Symposium Conference Record, IEEE 2011, pp. 1927–1929.

[34] Y. Wu, F. Meng, Q. Li, M. Koschan, C.L. Melcher, Phys. Rev. Appl. 2 (2014), 044009.
[35] N. Cherepy, Z. Seeley, S. Payne, P. Beck, O. Drury, S. O'Neal, K.M. Figueroa, S. Hunter, L. Ahle, P. Thelin, IEEE Trans. Nucl. Sci. 60 (2013) 2330–2335.
[36] Y. Wang, G. Baldoni, C. Brecher, W.H. Rhodes, U. Shirwadkar, J. Glodo, I. Shah, C. Ji, Properties of transparent (Gd, Lu) 3 (Al, Ga) 5O12: Ce ceramic with Mg, Ca and Ce co-dopants. Medical Applications of Radiation Detectors V, SPIE,, 2015, pp. 50–57.
[37] X. Chen, H. Qin, Y. Zhang, J. Jiang, Y. Wu, H. Jiang, J. Eur. Ceram. Soc. 37 (2017) 4109–4114.
[38] P. Sibczynski, J. Iwanowska-Hanke, M. Moszyński, L. Swiderski, M. Szawłowski, M. Grodzicka, T. Szczęśniak, K. Kamada, A. Yoshikawa, Nucl. Instrum. Methods Phys. Res. Sect. A Accel. Spectrom. Detect. Assoc. Equip. 772 (2015) 112–117.
[39] S. Chen, H. Wei, C.L. Melcher, Y. Wu, Opt. Mater. Express 3 (2013) 2022–2027.
[40] W. Chewpraditkul, L. Swiderski, M. Moszynski, T. Szczesniak, A. Syntfeld-Kazuch, C. Wanarak, P. Limsuwan, Phys. Status Solidi A Appl. Mater. Sci. 206 (2009) 2599–2605.
[41] X. Chen, H. Qin, Y. Zhang, Z. Luo, J. Jiang, H. Jiang, J. Am. Ceram. Soc. 98 (2015) 2352–2356.
[42] J.-Y. Zhang, Z.-H. Luo, Y.-F. Liu, H.-C. Jiang, J. Jiang, G.-Q. Liu, J.-X. Zhang, H.-M. Qin, J. Eur. Ceram. Soc. 37 (2017) 4925–4930.
[43] G. Zorloni, F. Cova, M. Caresana, M. Di Benedetto, J. Hostaša, M. Fasoli, I. Villa, I. Veronese, A. Fazzi, A. Vedda, Radiat. Meas. 129 (2019), 106203.
[44] M. Kalyani, S. Tyagi, A.K. Rawat, T. Singh, P.S. Patel, S.S. Sarkar, G.A. Desai, Kumar, IEEE Trans. Nucl. Sci. 67 (2020) 2415–2420.
[45] X. Chen, H. Qin, X. Wang, C. Yang, J. Jiang, H. Jiang, J. Eur. Ceram. Soc. 36 (2016) 2587–2591.
[46] J. Li, Y. Wu, Y. Pan, W. Liu, L. Huang, J. Guo, Int. J. Appl. Ceram. Technol. 5 (2008) 360–364.
[47] I. Pricha, W. Rossner, R. Moos, J. Am. Ceram. Soc. 99 (2016) 211–217.
[48] C. Hu, Y. Shi, X. Feng, Y. Pan, Opt. Express 23 (2015) 18243–18255.
[49] K. Shimazoe, A. Koyama, H. Takahashi, T. Ganka, P. Iskra, A. Marquez Seco, F. Schneider, F. Wiest, Nucl. Instrum. Methods Phys. Res. Sect. A Accel. Spectrom. Detect. Assoc. Equip. 873 (2017) 12–15.
[50] K. Shimazoe, A. Choghadi, H. Takahashi, K. Watanabe, IEEE Trans. Nucl. Sci. 63 (2016) 679–684.
[51] T. Kobayashi, S. Yamamoto, S. Okumura, J.Y. Yeom, K. Kamada, A. Yoshikawa, Nucl. Instrum. Methods Phys. Res. Sect. A Accel. Spectrom. Detect. Assoc. Equip. 842 (2017) 14–19.
[52] R. Coulon, V. Kondrasovs, Q. Lecomte, J. Dumazert, Radiat. Meas. 117 (2018) 57–62.
[53] M.N. Ullah, C. Park, E. Pratiwi, C. Kim, H. Choi, J.-Y. Yeom, Nucl. Instrum. Methods Phys. Res. Sect. A Accel. Spectrom. Detect. Assoc. Equip. 946 (2019), 162631.
[54] T. Huang, Q. Fu, C. Yuan, S. Lin, Nucl. Instrum. Methods Phys. Res. Sect. A Accel. Spectrom. Detect. Assoc. Equip. 881 (2018) 48–52.
[55] J. Hostaša, F. Cova, A. Piancastelli, M. Fasoli, C. Zanelli, A. Vedda, V. Biasini, Fabrication and luminescence of Ce-doped GGAG transparent ceramics, effect of sintering parameters and additives, Ceram. Int. 45 (2019) 23283–23288, https://doi.org/10.1016/j.ceramint.2019.08.025.
[56] M. Asadian, S.H. Seyedein, M.R. Aboutalebi, A. Maroosi, J. Cryst. Growth 311 (2009) 342–348.
[57] M. Wei, L. Zhang, Sci. Rep. 8 (2018).
[58] J.P. Hollingsworth, J.D. Kuntz, T.F. Soules, J. Phys. D Appl. Phys. 42 (2009), 052001.
[59] H. Mehrer, Diffusion in Solids: Fundamentals, Methods, Materials, Diffusion-controlled Processes, Springer Science & Business Media,, 2007.
[60] D. Cherniak, Phys. Chem. Miner. 26 (1998) 156–163.
[61] H. Yagi, K. Takaichi, K.-i Ueda, Y. Yamasaki, T. Yanagitani, A. Kaminskii (-), LASER Phys. Lawrence 15 (2005) 1338.
[62] R. Boulesteix, A. Maitre, J.-F. Baumard, Y. Rabinovitch, C. Sallé, S. Weber, M. Kilo, J. Eur. Ceram. Soc. 29 (2009) 2517–2526.
[63] T. Kornher, K. Xia, R. Kolesov, N. Kukharchyk, R. Reuter, P. Siyushev, R. Stöhr, M. Schreck, H.-W. Becker, B. Villa, Appl. Phys. Lett. 108 (2016), 053108.
[64] N.J. Everall, Appl. Spectrosc. 63 (2009) 245A–262A.
[65] N.J. Everall, Analyst 135 (2010) 2512–2522.
[66] J. Hubbell, S. Seltzer, Gaithersburg, MD: National Institute of Standards and Technology, (1996).
[67] G. Vourlias, Coatings 10 (2020) 1005.